https://doi.org/10.5194/egusphere-2026-3516
Preprint. Discussion started: 3 September 2026

Quantifying area-source methane fluxes with path-averaged laser beam concentration measurements and Bayesian inversion

Elijah A. Miller[1], Sean Coburn[1, 2], Caroline Alden[2,3], Kevin Rozmiarek[4], Daven Henze[1], Tyler R. Jones[4], and Gregory B. Rieker[1, 2]
[1]Mechanical Engineering, University of Colorado Boulder, Boulder, CO 80309, USA
[2]LongPath Technologies, Inc., Boulder, CO 80301, USA
[3]Cooperative Institute for Research in Environmental Sciences, University of Colorado Boulder
[4]Institute of Arctic and Alpine Research, University of Colorado Boulder, Boulder, CO 80309, USA

Correspondence: Elijah Miller (eli.miller@colorado.edu)

Abstract. Accurate quantification of diffuse, area-source methane emissions remains a key challenge in closing the gap between bottom-up and top-down estimates of the global methane budget. Existing measurement approaches are limited by spatial coverage and ability to interrogate diffuse sources in the presence of a time-varying background concentration. Here, we present a framework combining kilometer-scale path-averaged laser beam concentration measurements with an analytical Bayesian inverse modeling approach to simultaneously retrieve spatially distributed area-source methane fluxes and a time-varying background concentration, without requiring direct background subtraction. We evaluate the system through an Observing System Simulation Experiment (OSSE) using real meteorological data, realistic instrument and transport model error, and a representative laser beam geometry observing three distinct but diffuse area sources. The inversion framework accurately retrieves weekly average emission rates across a wide range of flux magnitudes, with well-constrained estimates achievable for near-beam sources at median concentration enhancements as low as 1 ppb above background. We demonstrate the utility of running an ensemble of inversions to provide more robust emission estimates in the presence of uncertain prior flux distribution parameters. The system maintains accuracy within 10% flux sources characterized in the prior even when a nearby emitting source is not represented in the prior estimate. This framework expands the conditions over which path-averaged laser concentration measurements can be used for area-source emission quantification and provides a pathway for optimizing future real-world deployments.

1 Introduction

Accurate measurement of greenhouse gas fluxes aids our understanding of carbon cycle dynamics, which is key to developing climate change mitigation strategies. Second to carbon dioxide, methane contributes significantly to climate change, with a global warming potential of 27-30 relative to CO_2 over a 100-year time horizon (Intergovernmental Panel on Climate Change (IPCC) 2023). Mitigating methane emissions presents an important opportunity to limit near-term climate impacts from human-induced warming (Ocko et al., 2021). Saunois et al. (2025) highlighted the need for better methane flux information at local to regional scales (1-100+ km^2) and demonstrated that the largest uncertainties in methane emissions remain for natural source categories, which are typically characterized by spatially diffuse emissions. For example, divergent estimates of net methane flux between top-down (atmospheric inversions of concentration data) and bottom-up (data-driven upscaling of site-specific fluxes) remain in the northern permafrost region, where lake and wetland area sources dominate emissions (Hugelius et al. 2024). Although not a natural source category, recent studies have also highlighted discrepancies between estimated and observed emissions in anthropogenic area-source emissions such as landfills (Dogniaux et al. 2025). The diffuse nature of methane fluxes from distributed area sources presents challenges in local-scale flux quantification. Area sources produce smaller concentration enhancements than point sources for the same flux (Jacob et al. 2022, 2016; Venkatram and Thiruvenkatachari 2023), and spatial flux heterogeneity requires quantification at high spatial resolution to ensure accurate emissions estimates (Hashemi et al. 2025). For example, area-source fluxes from lakes (Rosentreter et al. 2021), agricultural plots (Qian et al. 2023), landfills (Mønster, Kjeldsen, and Scheutz 2019), mines (Karacan et al. 2024), are difficult to quantify, but are significant contributors to the global carbon budget (Saunois et al. 2025). Understanding and measuring net fluxes at the landscape scale (larger than a single emitting feature, but smaller than regional scale) and with high (hourly to seasonal) temporal resolution has successfully addressed the discrepancies between top-down and bottom-up emission estimates in the Oil and Gas sector (Vaughn et al. 2018; Tibrewal et al. 2024; Johnson, Conrad, and Tyner 2023; Zavala-Araiza et al. 2015),. An opportunity remains for novel measurements and methods to make similar advancements in measuring area methane sources.

Particularly for area sources with diffuse emission, existing measurement technologies suffer from limited spatial extent (e.g., flux chambers, eddy covariance towers) (Hu et al. 2014), are point-in-time with limited detection threshold for area source fluxes (e.g., airborne eddy covariance or imaging spectrometers) (Kohnert et al. 2018; Elder et al. 2021), or do not resolve landscape heterogeneity at scales necessary to improve mechanistic understanding of emissions (e.g. area flux mapping satellites) (Jacob et al. 2022). Additionally, global estimates of greenhouse gas fluxes suffer from limited data, especially in difficult-to-deploy locations such as the Arctic and Tropics (Pallandt et al. 2025; Kuhn et al. 2021). Thus, a method capable of resolving flux heterogeneity at fine spatial scales while covering areas large enough to assess net ecosystem fluxes remains an unmet need.

Long open-path laser spectrometers have shown recent advancements for measuring fluxes of trace gases from both point sources (Coburn et al. 2018; Alden et al. 2019; IJzermans et al. 2024; Hirst et al. 2020), and distributed area sources (Herman et al. 2021; T. Flesch et al. 2016; You et al. 2021; Pernini et al. 2022; Thomas K. Flesch et al. 2023). While recent studies have estimated methane emissions from diffuse area sources, existing methods tend to look at a low number of isolated source areas and require a dedicated measurement of "background" concentration, usually measured upwind of the source(s) of interest. Previous studies remove data where such background subtraction was not possible due to unfavorable wind direction (Thomas K. Flesch et al. 2023). These constraints have led to estimating emissions from systems with well-defined source boundaries and prohibited emissions quantification in systems characterized by a network of diffuse area sources in proximity.

https://doi.org/10.5194/egusphere-2026-3516
Preprint. Discussion started: 3 September 2026

Current studies often calculate independent flux estimates at short time intervals (i.e., 30 minutes) which restricts methods to "well-posed" problems (i.e. # measurements ≥ # unknown flux rates) in a given inversion time period (Crenna, Flesch, and Wilson 2008; Thomas K. Flesch et al. 2009). Application of Bayesian methodologies helps regularize the inversion problem, allowing quantification of ill- or poorly conditioned flux quantification problems (Yee and Flesch 2010). Hirst et al. (2020) demonstrated simultaneously solving for emission rates and a background concentration without explicit background subtraction by using Bayesian inversion; however, this method was specifically designed to retrieve sparse point-source emissions in oil and gas settings. The full framework of analytical Bayesian flux inversion using path-averaged laser beam concentration measurements presents an unexplored avenue for area-source flux estimation. Benefits of the analytical Bayesian inversion framework include the ability to solve for large spatio-temporal state vectors efficiently without the limitations of only tackling problems traditionally regarded as "well-posed". Additionally, by considering sources of error in the inversion, flux estimates include a built-in characterization of their uncertainty and independence.

We present an Observing System Simulation Experiment (OSSE) to demonstrate a Bayesian inversion system capable of accurately retrieving surface-to-atmosphere methane fluxes of large area sources using path-averaged laser beam concentration measurements. We simultaneously retrieve spatially distributed area-source fluxes without directly subtracting background concentrations. The use of a Bayesian inversion framework increases the amount of concentration data incorporated in a single flux estimate, and we avoid filtering out time periods with a "contaminated" background measurement. We assess the ability of our inversion system's performance over a range of flux (and therefore measured concentration) magnitudes and explore the limitations of such an inversion system. Finally, we explore the effects of using an incomplete prior flux estimate and show the robustness of the inversion system to uncharacterized, nearby sources in the prior. Results from this study informs future measurement campaigns and determine the limits of using kilometer-scale laser spectrometers for measuring diffuse area-source methane fluxes.

2 Methods

The following sections detail the fundamentals of the Bayesian inversion (Section 2.1), and the atmospheric transport model (Section 2.2). We then simulate a domain comprising multiple, diffuse area-sources; given a true surface flux distribution, we generate enhancements (concentration increments due to the local surface fluxes above a background concentration), add uncertainty and a simulated background concentration, resulting in synthetic measurements (Section 2.3). We choose to simulate synthetic concentration data to control variables in the OSSE, isolate their influence, and assess the accuracy and precision of our inversion system's flux estimates. (Section 2.4). Finally, we set up four experiments designed to assess the inversion system's capabilities across a range of flux strengths, and in the presence of imperfect *a prior* knowledge of source locations.

https://doi.org/10.5194/egusphere-2026-3516
Preprint. Discussion started: 3 September 2026

2.1 Solution to the Bayesian inverse problem

We infer a vector of time-averaged surface fluxes $\vec{x}_{\text{flux}} \in \mathbb{R}^n$ given the vector of path-averaged laser beam concentration measurements $\vec{z} \in \mathbb{R}^m$, where n is the number of pixels in our domain, m is the product of the number of laser beams, b, and the number of transport model time steps t. Enhancements above background $\vec{z}_{\text{enhancement}}$ with normally-distributed errors ϵ are mapped via atmospheric transport-observation Jacobian $\mathbf{H}_{\text{flux}}$, comprising laser beam concentration footprints as computed with the backward Lagrangian stochastic (BLS) atmospheric dispersion model (Section 2.2).

$$\vec{z}_{\text{enhancement}} = \mathbf{H}_{\text{flux}}\,\vec{x}_{\text{flux}} + \vec{\epsilon}$$

In diffuse-flux quantification scenarios, it may not be possible to directly measure background concentrations that are not variably influenced by fluxes from nearby sources. In this case, we work directly with raw concentration measurements $\vec{z}$ rather than enhancements $\vec{z}_{\text{enhancement}}$. We augment the state vector $\vec{x}$ to simultaneously solve for the unknown fluxes $\vec{x}_{\text{flux}}$ and a vector of time-varying background concentrations $\vec{x}_{\text{background}} \in \mathbb{R}^t$. We augment $\mathbf{H}$ with a block-diagonal matrix of ones $\mathbf{H}_{\text{background}}$ to encode the assumption that the background concentration is spatially uniform (i.e., measured identically by all laser beams), but can vary in time.

$$\begin{aligned}\vec{z} &= \vec{z}_{\text{enhancement}} + \vec{z}_{\text{background}} \\ &= [\mathbf{H}_{\text{flux}} \quad \mathbf{H}_{\text{background}}]\begin{bmatrix}\vec{x}_{\text{flux}} \\ \vec{x}_{\text{background}}\end{bmatrix} + \vec{\epsilon}\end{aligned}$$

To regularize the potentially ill-posed inversion problem, we assume a prior distribution of the state vector $\vec{x}_a$, a corresponding prior error covariance matrix $\mathbf{S}_a$, and an observational error covariance matrix $\mathbf{S}_o$. In this study, we assume fluxes are constant over the duration of the experiment and optimize scaling factors on the prior. Because we solve for scaling factors, the entries in the prior error covariance matrix are defined relative to the prior. We define prior error covariance matrices with off-diagonal correlation structure to enforce spatial and temporal correlation in the inversion solution.

We solve for the optimal estimate of the state vector $\vec{x}$ (scaling factors on flux and background concentrations) by minimizing the cost function (Rodgers 2000; Brasseur and Jacob 2017):

$$J(\vec{x}) = (\vec{x} - \vec{x}_a)^\top \mathbf{S}_a^{-1}(\vec{x} - \vec{x}_a) + (\vec{z} - \mathbf{H}\vec{x})^\top \mathbf{S}_o^{-1}(\vec{z} - \mathbf{H}\vec{x}),$$

To reduce the rank of the state vector and improve conditioning, we solve the inverse problem through an eigen decomposition of the prior-preconditioned Hessian $\widehat{\mathbf{G}}_p$(Bousserez and Henze 2018):

$$\widehat{\mathbf{G}}_p \equiv \mathbf{S}_a^{1/2}\mathbf{H}^\top\mathbf{S}_o^{-1}\mathbf{H}\mathbf{S}_a^{1/2} = \mathbf{V}\mathbf{\Lambda}\mathbf{V}^\top,$$

where the eigen decomposition introduces orthonormal eigenvectors $\mathbf{V}$ and eigenvalues $\mathbf{\Lambda}$.

We truncate to the k leading eigenmodes to regularize the solution. We select k to preserve all eigenvalues greater than unity, after which the eigenmodes are assumed to be exclusively informed by the prior (Bousserez and Henze 2018). The solution to the Bayesian inversion problem is given by:

$$\mathbf{A} = \mathbf{S}_a^{1/2}\mathbf{V}_k\mathbf{\Lambda}_k(\mathbf{I}_k + \mathbf{\Lambda}_k)^{-1}\mathbf{V}_k^\top\mathbf{S}_a^{-1/2}.$$

https://doi.org/10.5194/egusphere-2026-3516
Preprint. Discussion started: 3 September 2026

where $\mathbf{A}$ is the averaging kernel matrix, subscript k indicates eigenmode truncation, and $\mathbf{I}$ is the identity matrix. The error covariance of the posterior state vector, $\hat{\mathbf{S}}$, is:

$$\hat{\mathbf{S}} = (\mathbf{I} - \mathbf{A})\mathbf{S}_a,$$

and the full-rank posterior state vector estimate, $\hat{\vec{x}}$, is:

$$\hat{\vec{x}} = \vec{x}_a + \hat{\mathbf{S}}\mathbf{H}^\top \mathbf{S}_o^{-1}(\vec{z} - \mathbf{H}\vec{x}_a).$$

The averaging kernel gives a measure of how much the posterior estimate is informed by the prior estimate versus the observations. We can calculate the total degrees of freedom for signal (DOFS) of the inversion as the trace of the averaging kernel matrix. The DOFS represents the number of independent pieces of information constrained by the observations (Rodgers 2000). Because our inversion state vector contains both unknown flux values and background concentrations, we decompose the total DOFS into contributions from the state vector elements corresponding to flux ($\mathrm{DOFS}_{\mathrm{flux}}$) and background concentration ($\mathrm{DOFS}_{\mathrm{bg}}$).

$$\mathrm{DOFS} = \mathrm{DOFS}_{\mathrm{flux}} + \mathrm{DOFS}_{\mathrm{bg}} = \mathrm{tr}(\mathbf{A})$$

We additionally calculate the posterior error reduction in each pixel as $\left(1 - \frac{\hat{\sigma}}{\sigma_a}\right)$ where $\hat{\sigma}$ and σ_a are the square root of the diagonal elements of the posterior and prior covariance matrices, respectively. High values of error reduction (i.e. 100 %) indicate that the inversion improves our confidence in the flux estimates over the prior.

2.1.1 Aggregation to smaller state

The high resolution of the inversion solution allows attribution of area-averaged fluxes, accounting for the covariance structure in the inverse solution (Nesser et al. 2024). When characterizing fluxes from area sources, we are interested in area-average fluxes, rather than flux at a single pixel, which may not be constrained by the observations. We use a mapping matrix $\mathbf{W} \in \mathbb{R}^{p \times n}$ where p is the number of regions where we wish to summarize our inversion results. We normalize the rows of $\mathbf{W}$ to unity to calculate the area-averaged flux, rather than total emission rate. We can calculate the reduced-dimension posterior estimate $\hat{\vec{x}}_{\mathrm{reduced}}$, posterior covariance matrix, $\hat{\mathbf{S}}_{\mathrm{reduced}}$, and averaging kernel matrix $\mathbf{A}_{\mathrm{reduced}}$ as:

$$\hat{\vec{x}}_{\mathrm{reduced}} = \mathbf{W}\hat{\vec{x}}$$

$$\hat{\mathbf{S}}_{\mathrm{reduced}} = \mathbf{W}\hat{\mathbf{S}}\mathbf{W}^{\mathrm{T}}$$

$$\mathbf{A}_{\mathrm{reduced}} = \mathbf{W}\mathbf{A}\mathbf{W}^{*}$$

Where $\mathbf{W}^{*}$ is the Moore-Penrose pseudoinverse.

2.2 Atmospheric transport and source-receptor relationship (H) calculation

We simulate atmospheric transport and source-receptor relationships using BLS modeling (Thomas K. Flesch, Wilson, and Yee 1995; T. K. Flesch et al. 2004; Kljun, Rotach, and Schmid 2002). In the BLS model, simulated particles are released from a receptor (sensor) location and transported backward in time, assuming a statistically stationary atmospheric state. The

https://doi.org/10.5194/egusphere-2026-3516
Preprint. Discussion started: 3 September 2026

model calculates many particles' trajectories with a Langevin equation where the evolution parameters are determined using the vertical wind profile (determined from the mean wind vector $\bar{u}$, friction velocity u^*, and Obukhov length L) and standard deviations of the wind components $\sigma_u, \sigma_v, \sigma_w$ (Thomas K. Flesch, Wilson, and Yee 1995). The particles touchdowns with the surface are cataloged and used to derive the source-receptor relationship (C/Q)_sim, or area-integrated concentration "footprint" between a given receptor location and source area,

$$(C/Q)_{\mathrm{sim}} = \frac{1}{N}\sum_{\mathrm{area}} \left|\frac{2}{w_0}\right|$$

.

For a given source area and measurement location, the increment of measured concentration (C) per unit flux (Q) is given as the sum of particles with touchdowns in the area, weighted by the inverse of their touchdown velocity (w_0) and normalized by the number of simulated particles (N) (Thomas K. Flesch, Wilson, and Yee 1995). This source-receptor relationship accounts for the effects of measurement geometry and meteorology on a concentration measurement.

To compute source-receptor relationships for path-averaged laser measurements, we discretize each laser beam into equally spaced point receptors and average their individual footprints. The result is a concentration footprint for each path-averaged laser beam concentration measurement at each time step of the BLS model, with units [s $\;$ m^{-3}] (Vesala et al. 2008). To reduce the number of touchdowns required for accurate footprint computation, we use kernel density estimation (KDE) methods to calculate each laser beam's path-averaged concentration footprint from the BLS-generated touchdowns (Haan 1999; Kljun, Rotach, and Schmid 2002).

BLS touchdown coordinates often exhibit highly anisotropic spatial distributions, with much more spread in the along-wind than the cross-wind direction (Kljun, Rotach, and Schmid 2002). Spectral KDE methods scale efficiently with a large number of touchdowns and pixels. A limitation of these methods is that they require the use of fixed-bandwidth, radially symmetric kernels that cannot simultaneously resolve the narrow crosswind touchdown distribution without under-smoothing the long, along-wind tail. (Fan and Marron 1994; Odland 2018). To allow the use of such methods with anisotropic BLS touchdown data, we pre-whiten our touchdown coordinates to have an identity covariance matrix before fitting the kernel estimate (Silverman 1998; Fukunaga 2009). Our footprint estimate from the KDE on the whitened data is then transformed back to the original touchdown data coordinates. With this method, we avoid multiple computations of the kernel density as done in previous methods with the adaptive bandwidth method (Kljun, Rotach, and Schmid 2002).

2.3 Observing system simulation experiment (OSSE) setup

We use an OSSE to demonstrate the applicability of the above-described framework where we use laser beam concentration footprint functions and Bayesian flux estimation methods to estimate area source surface-to-atmosphere fluxes in the presence of time-varying background concentrations. In the OSSE, we generate synthetic laser beam path-averaged enhancement from a set of synthetic "true" fluxes, apply instrument and transport model error, and evaluate our ability to

https://doi.org/10.5194/egusphere-2026-3516
Preprint. Discussion started: 3 September 2026

accurately retrieve the true fluxes. We assess the success of the inversion based on 1) how well we can retrieve the correct flux rate from the source regions and 2) how well we can determine that the flux rates of the non-source regions are zero.

2.3.1 Spatial Domain

The observed domain is a 4450 by 2450 m region with simulated surface fluxes from three equally sized 500 m by 500 m area sources, distributed across the simulation domain. We simulate the underlying resolution of the spatial flux distributions and footprint calculations on a grid of pixels with 50 m resolution. We design these sources to simulate area-source fluxes where we aim to resolve flux heterogeneity without a clean background concentration measurement. The simulated observing system comprises a single laser transceiver with 9 radially-oriented laser beams, (one-way pathlengths of 1000 m), each capable of measuring a path-averaged methane concentration, such as with absorption spectroscopy (Fig. 1) (Han et al., 2024; Schmitt et al., 2023; Alden et al., 2020; Nikodem et al., 2015; Rieker et al., 2014; Thoma et al., 2005). We simulate each path with a constant height of 2 m above ground level.

https://doi.org/10.5194/egusphere-2026-3516
Preprint. Discussion started: 3 September 2026

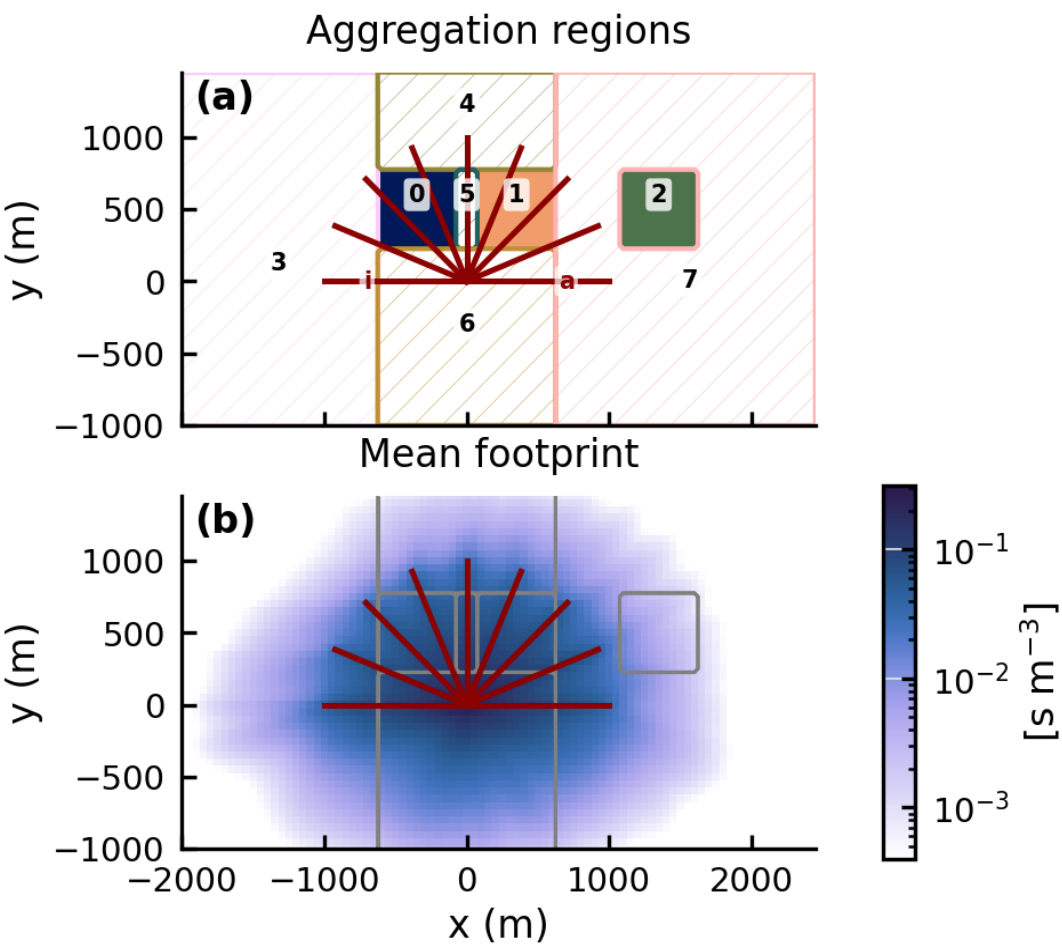

200 **Figure 1** Spatial setup of the OSSE. (a) Dark red lines indicate the laser beam geometry radiating from the central laser transceiver location. Beams are labeled a-I moving counterclockwise from the positive x direction. Aggregation regions (Section 2.1.1) used for flux estimation are shown in different colors and numbered 0-7. Source (emitting) regions 0, 1, and 2 are indicated with solid colors, while non-source regions 3-7 are shown with hatching. (b) Mean footprint sensitivity averaged across all time periods and beams, showing the spatial distribution of measurement sensitivity.

We define 8 regions over which we assess the accuracy of our inversion system. These include three source regions (regions 0, 1, and 2) where we simulate non-zero surface-to-atmosphere fluxes of methane and five non-source regions (regions 3, 4, 5, 6, and 7) where we do not simulate the surface-to-atmosphere release of gas (see Fig. 1). Region 5 is a narrow buffer zone between regions 0 and 1, and region 7 encompasses the rightmost portion of the domain, excluding the area occupied by region 2. A summary of the coordinates of each region is provided in Table 1.

Table 1: Summary of aggregation region coordinates and properties. *Region 7 is bounded by the domain corners, excluding the area occupied by region 2

Region	Bottom-left (x, y) (m)	Top-right (x, y) (m)	Area (m^2)	Type
0	$(-600, +250)$	$(-100, +750)$	302 500	Emitting

https://doi.org/10.5194/egusphere-2026-3516
Preprint. Discussion started: 3 September 2026

Region	Bottom-left (x, y) (m)	Top-right (x, y) (m)	Area (m^2)	Type
1	$(+100, +250)$	$(+600, +750)$	302 500	Emitting
2	$(+1100, +250)$	$(+1600, +750)$	302 500	Emitting
3	$(-2000, -1000)$	$(-650, +1450)$	3 500 000	Non-emitting
4	$(-600, +800)$	$(+600, +1450)$	875 000	Non-emitting
5	$(-50, +250)$	$(+50, +750)$	82 500	Non-emitting
6	$(-600, -1000)$	$(+600, +200)$	1 562 500	Non-emitting
7	$(+650, -1000)$	$(+2450, +1450)$	4 322 500	Non-emitting*

Two of the simulated area sources (regions 0 and 1) are inscribed within the angular sweep of the laser beams, while region 2 is located exterior to this area. We test the ability of our inversion system to correctly infer fluxes from region 0 and region 1, even in the presence of emissions from the nearby region 2.

The laser transceiver is oriented so that some beams are located predominantly upwind of the area sources for the given meteorology (see Fig. 2). This mimics reality, wherein local meteorology patterns may be known ahead of a deployment and used to inform the sensor location and orientation. We orient the laser beams to minimize enhancement on some beams (0 and 8), to capture minimally enhanced concentration measurements or background conditions.

2.3.2 True flux strengths ($\vec{x}_{\mathrm{flux,true}}$)

We simulate a range of synthetic "true" surface-to-atmosphere flux strengths (and therefore a range of simulated concentration enhancements measured by the laser beams) and assess the inversion system's flux quantification accuracy under each condition. For each source strength value, we define a reference concentration enhancement level, called the "median enhancement level", or the median concentration enhancement value on the beam with the highest overall concentration enhancement value. Emitting area flux rates range from 7.14×10^{-2} g m^{-2} s^{-1} to 7.14×10^{4} g m^{-2} s^{-1}, which are chosen to produce median enhancements ranging from 0.1 ppb to 100 ppm. In this study, beam "d" (Fig. 1) consistently demonstrates the highest concentration enhancement value, due to the meteorology and orientation of the sensor with respect to the source locations. We assume a uniform flux rate across each of the source regions in space and time. A summary of flux strengths, resulting enhancements, and other relevant metrics are summarized in Table 2.

Table 2: Summary of simulated flux levels and corresponding observing system characteristics used in Experiments 3 and 4. Median enhancement refers to the median concentration enhancement on beam "d" over the 7-day simulation period.

Flux	Median enhancement	SNR	Dominant error source
(g m^{-2} s^{-1})	(ppb)		
7.14×10^{-2}	0.1	0.01	Instrument

https://doi.org/10.5194/egusphere-2026-3516
Preprint. Discussion started: 3 September 2026

7.14×10^{-1}	1		0.14	Instrument
7.14×10^{0}	10		1.4	Instrument
7.14×10^{1}	100		14	Transport model
7.14×10^{2}		1×10^{3}	143	Transport model
7.14×10^{3}		1×10^{4}	1430	Transport model
7.14×10^{4}		1×10^{5}	14300	Transport model

2.3.3 True background concentrations ($\vec{x}_{\mathbf{background,true}}$)

We generate a synthetic background concentration ($\vec{z}_{\text{background, true}}$) timeseries to be added to the synthetic enhancements measured by our laser beams. We assume that background fluctuations are driven by a combination of diurnal and synoptic components (Padilla et al. 2024); however, we note that for real studies, site-specifics will alter the character of background concentration variation (Metya et al. 2021; K. Patra et al. 2009).

We generate a synthetic timeseries by summing two band-pass-filtered white noise components: a synoptic component with periods of 12 hours to 100 days and a diurnal component with periods of 23-25 hours with twice the amplitude of the synoptic component. The goal of this timeseries construction is to roughly approximate variations in background concentration due to advection of regional sources and diurnal changes due to boundary layer dynamics. Both components are transformed to the time domain via inverse Fourier transform. The combined timeseries is scaled to have a mean concentration of 2000 ppb and standard deviation of 20 ppb, representative of typical methane background concentrations and variability (Thoning et al. 2022). The resulting background timeseries is shown in panel (a) of Fig. 2.

2.3.4 Synthetic (true) enhancements ($\vec{z}_{\mathbf{enhancement,true}}$)

We create pseudodata for the inversion using the true fluxes convolved with footprints. To generate synthetic atmospheric concentration data, we simulate atmospheric transport using real meteorological data. The use of measured rather than simulated meteorological data ensures realistic correlation between variables that otherwise may be difficult to parameterize. Mean wind and turbulence parameters are generated from sonic anemometer (RM Young 81000) measurements deployed at the Platteville Atmospheric Observatory (40.181940 N, -104.725730 W) in Colorado, USA at 3m above ground level between February 5-13th, 2020. Data are collected at 32 Hz and averaged to 30 minutes as the underlying assumptions of the BLS dispersion model are only valid when assuming a stationary atmospheric state (T. Flesch et al. 2005). Input data for the BLS simulation include wind vector $\bar{U}$, friction velocity u^{*}, and standard deviations of rotated wind velocity components $\sigma_u, \sigma_v, \sigma_w$, all calculated from the sonic anemometer data (Aubinet, Vesala, and Papale 2012). We assume a constant value of Obukhov length of $L = \infty$ representing neutral stability. We calculate wind direction rotation following the double rotation method (Aubinet, Vesala, and Papale 2012). A wind rose for the meteorology used to derive synthetic enhancements can be found in Fig. S1. We simulate laser beam concentration footprints for each 30-minute period within 1 week with the BLS

https://doi.org/10.5194/egusphere-2026-3516
Preprint. Discussion started: 3 September 2026

method. As described in Section 2.2, we discretize the line sensors (laser paths) into 50 equally spaced segments when calculating footprints. Footprints are calculated using 5000 BLS release particles per discretized laser beam segment with a maximum horizontal particle tracking distance of 1000 m.

For each beam and timestep, we compute the enhancements due to the true flux $\vec{x}_{\text{flux, true}}$ by integrating the product of each beams' concentration footprint function and the spatial flux distribution (Vesala et al. 2008). Example enhancements on beam "d" (which is positioned directly atop the source regions) resulting from a true flux value of 7.14 g m^{-2} s^{-1} are shown in comparison to a primarily unenhanced "background" beam "i" (which is positioned furthest from the source regions) in Fig. 2, (b).

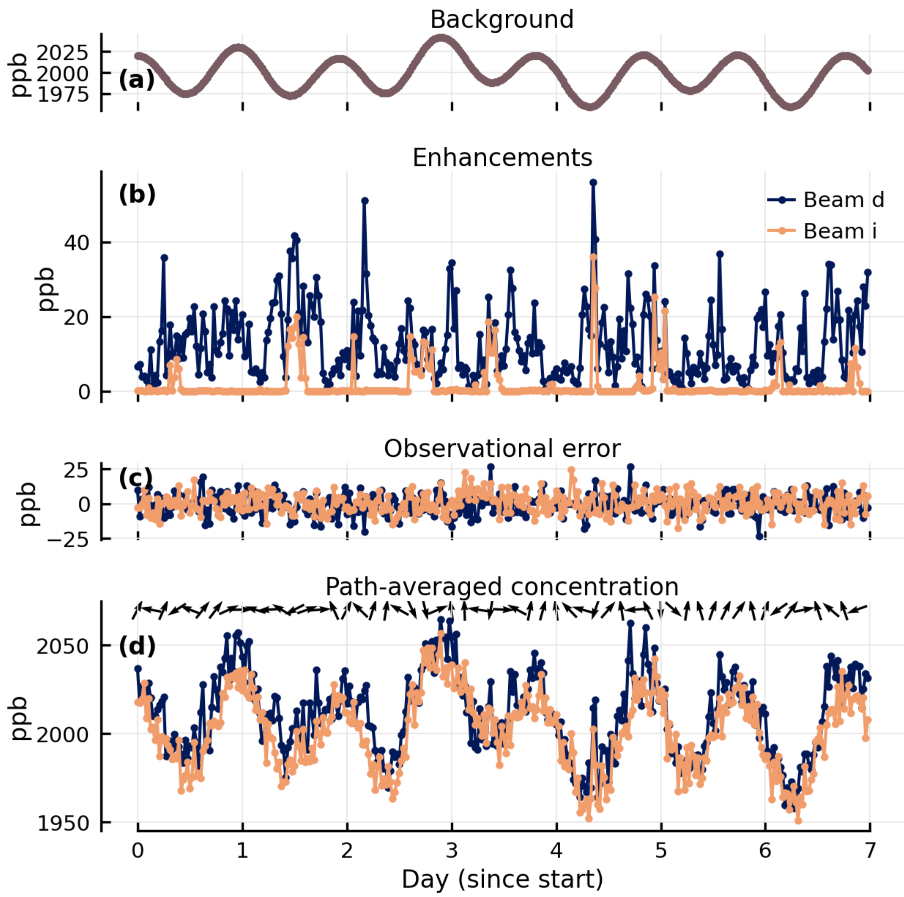

Figure 2: Simulated 30-minute concentration timeseries for the highest and lowest median-enhancement beams over the 7-day measurement period. (a) Background methane concentration, showing diurnal and synoptic variation. (b) Synthetic enhancements due to all emitting regions, which vary with wind direction and beam location. (c) Observational error representing instrument and transport model error. (d) Total signal measured on each beam, combining background, enhancements due to local sources, and observational error. Wind direction arrows in panel (d) indicate the meteorological wind direction at 6-hour intervals.

https://doi.org/10.5194/egusphere-2026-3516
Preprint. Discussion started: 3 September 2026

2.3.5 Simulated observation errors

We simulate errors to represent realistic simulation of an imperfect observing system. We assume that uncertainties in our observations stem from both the instrument and the BLS atmospheric transport model.

To simulate the effect of measurement error, we add Gaussian random measurement error with standard deviation of 7 ppb for each beam. This is commensurate with state-of-the-art path-averaged concentration uncertainty for the detection of methane near ambient concentrations (Waxman et al. 2017). Instrument errors are generated independently and are uncorrelated between laser beams and across time.

We rely on past research and assume that the sum of all transport model uncertainties is $\pm 20\%$ (T. K. Flesch et al. 2004; Tagliaferri et al. 2023; Caulton et al. 2018). We generate a zero-mean Gaussian noise term with a standard deviation equal to 20% of the simulated enhancement value for each synthetic observation. Thus, for each timestep, the transport model error distribution is Gaussian with variance proportional to the squared enhancement. In practice, this produces heteroskedastic errors; larger enhancements have proportionally larger uncertainty values, reflecting the proportional nature of transport model error. We assume that transport model error may be due to the net effect of unrepresented terrain, surface heterogeneity, uncertainties in the underlying parameterizations used in the BLS model, and flow variations that happen faster than the transport model averaging period. As a result, we assume that transport model error will manifest on all laser beams similarly. To encode this assumption, the same realization of transport model error is applied to all beams at each time step. Example observational error traces are shown in Fig. 2 (c)

Note that the instrument error, which is fixed as a scalar value in concentration units, is scaled differently than the model error, which is scaled proportionally to the enhancements. Therefore, with different magnitudes of flux (and correspondingly different levels of enhancements), different observational error terms (instrument versus model error) will dominate. We define signal-to-noise ratio (SNR) is the ratio of median enhancement to the instrument noise floor (7 ppb). In Table 2, the dominant error source indicates whether instrument noise or transport model uncertainty is the larger contribution to total observational error. For a graphical representation of uncertainty sources, see Fig. S2.

2.3.6 Synthetic concentration measurement ($\vec{z}$)

To compute the total concentration measured by each beam, we sum the background concentration, true enhancement, and observational error timeseries. Example synthetic concentration measurements are shown in Fig. 2 (d).

2.4 Inversion setup

Configuring the inversion requires assigning the parameters of the prior $\vec{x}_a$, its error covariance matrix $\mathbf{S}_a$, and the observational error covariance matrix $\mathbf{S}_o$. In this OSSE, although the true fluxes and errors are known by construction, we only incorporate information in the inversion using *a priori* assumptions about flux magnitudes, broad spatial and temporal structure, and observational uncertainties. These parameters will not all be perfectly known in a real study, especially when

https://doi.org/10.5194/egusphere-2026-3516
Preprint. Discussion started: 3 September 2026

defining prior flux mean and uncertainty. We use an ensemble of inversions to assess the sensitivity of our estimates to these prior choices.

2.4.1 Ensemble of Prior fluxes ($\vec{x}_a$)

Selection of prior fluxes can suffer from lack of objective observational data to support parameter selection. In regional- and continental-scale inversions, an inventory or other detailed bottom-up flux estimation is used to inform prior flux estimates. At local scales, prior flux estimates rely on ecosystem-specific meta-analyses (e.g. (Kuhn et al. 2021)), expert opinions, and the order of magnitude expected fluxes (Yee and Flesch 2010). To address the added source of uncertainty in assigning a prior flux estimate, we expand our solution to retrieve flux estimates from an ensemble of inversions.

We first categorize pixels as "source" or "non-source" when assigning the prior flux value and the prior uncertainty value. We then apply a percentage offset to the true flux to generate the prior flux estimate. Assigning a prior of zero to non-source pixels acts as an unintentional hard constraint; regardless of the retrieved scaling factor, the posterior estimate of a zero prior flux will be zero since we are retrieving a multiplicative scaling factor on the prior flux. Therefore, prior flux values for hypothesized non-emitting regions are small ($\pm 0.01\%$) compared to the true emitting flux, rather than zero.

For each of the source and non-source regions, we generate prior flux values as percentages of the true flux values. Three different prior flux values are used for source regions, and two different prior flux values are used for non-source regions (Table 3). The full factorial combination of these parameters yields 36 inversion members per flux level.

Table 3: Inversion ensemble parameter definitions. Each ensemble member is defined by selecting one value from each row.

Parameter	Possible Values		
Source region prior flux (relative to true flux)	75%	100%	125%
Source region prior flux uncertainty (relative to prior flux)	50%	75%	100%
Non-source region prior flux (relative to true flux)	0.1%	−0.1%	
Non-source region prior flux uncertainty (relative to prior flux)	100%	200%	

Variations in prior background concentration are not included as variables in the inversion ensemble. Background concentrations are a part of the state vector; however, we assume that the prior determination of a background concentration is a better-known quantity than fluxes. For example, analysis of measured concentrations by wind direction, gridded data assimilation products, or mean background concentration from nearby observation networks may provide reasonable approximations of the background for *a priori* use.

For state vector elements representing background concentrations, we assign a constant-in-time prior value of 2000 ppb.

2.4.2 Prior error covariance parameters ($\mathbf{S}_a$)

Prior error variances (squared diagonal elements of $\mathbf{S}_a$) for the flux state vector elements are determined for each inversion ensemble member as defined in Table 3. We set a prior uncertainty (square root of the variance) on the background

https://doi.org/10.5194/egusphere-2026-3516
Preprint. Discussion started: 3 September 2026

concentration of 1% (20 ppb), which captures the expected variability in the background concentration. As described in Section 2.3.3, site-specifics can determine the magnitude of background fluctuation to inform this choice for future studies. We can leverage additional *a priori* knowledge by encoding system-specific spatial and/or temporal structures into the prior error covariance matrix $\mathbf{S}_a$. Our use of off-diagonal terms in the prior error covariance matrix incorporates our hypothesis that our uncertainty in the fluxes is not spatially independent. This further imposes the constraint that the area-source fluxes we are trying to sense are diffuse and distributed over a broad area. Additionally, we assume that the errors in our static-assumed prior background concentration are correlated in time and that background concentrations vary slowly in time compared to the measured enhancements. To impose error covariance in space (for the flux values) and time (for the background values), we use a spherical covariance model (Wackernagel 2003; Miller et al. 2020), which decays to zero at the specified correlation length or time. Decay to zero allows for the use of sparse matrix storage and input/output for the prior error covariance matrix, improving numerical efficiency. For the prior error covariance of the flux pixels, we assume a correlation length of 1500 m between pixels defined *a priori* as "source" and a correlation length of 6000 m between pixels defined *a priori* as "non-source". We impose no prior error correlation between pixels defined *a priori* as "source" and "non-source". For state vector elements representing background concentrations, we use a correlation time of 1 day, assuming diurnal variation dominates background concentration variability from visual analysis of the measured pseudodata (Fig. 1 (d)). We assume no *a priori* correlations in error between flux and background components. For a real flux quantification study, off-diagonal prior error covariance parameters will be a function of the expected correlations in space and time of uncertainties in the prior flux and background concentrations, or could be determined with more sophisticated frameworks like Maximum Likelihood Estimation (Michalak et al. 2005).

2.4.3 Observational error covariance matrix ($\mathbf{S}_o$)

Proper assignment of observational error covariance parameters is imperative to ensure that the inversion doesn't over- or under-fit the observations. We assume no off-diagonal correlations in the observational error covariance matrix. In prescribing the diagonal of $\mathbf{S}_o$, we assume our measurements carry uncertainty to both instrument error and transport model error. We prescribe instrument error with a standard deviation of 7 ppb, which is the same value used to generate instrument noise. We assume that instrument uncertainties can be well-characterized in a real deployment. We use the prior flux estimate to calculate transport model uncertainty contributions to the $\mathbf{S}_0$ diagonal. We assume a transport model uncertainty equal to 20% of the enhancements predicted by the prior.

An undesirable side effect of under specifying the observational error is overfitting or underfitting the state vector to noise in the observations. Our inversion ensembles (as defined in Section 2.4.1) contain biased low and high priors, but we do not want biased-low priors to systematically suffer from overfitting the observations, and vice versa for the biased-high priors. As a result, we calculate transport model error for each beam and time step using the mean enhancement across all inversion ensemble members. The result is an observational error covariance matrix which is identical for all inversion members. Instrument and transport model uncertainties are added in quadrature to construct the diagonal of $\mathbf{S}_0$.

https://doi.org/10.5194/egusphere-2026-3516
Preprint. Discussion started: 3 September 2026

2.5 Experimental design

We undertake a series of observing system simulation experiments (OSSEs) aimed at assessing the performance of our inversion system. We progress with a series of increasingly complicated experiments. First, we evaluate the system with a single ensemble member and a single true flux strength to explore how uncertainty metrics from the Bayesian framework help contextualize the posterior estimate. We then use the full ensemble of inversions to examine what we expect is a more robust estimate of our flux uncertainties. Finally, we assess how these results scale across a range of true fluxes and conclude with assessing the robustness of the inversion system in the case of incomplete prior information.

2.5.1 Experiment 1: single ensemble member and true flux strength

In the first experiment, "single ensemble member", we assess outputs for a single inversion ensemble member to derive summary accuracy and uncertainty metrics. In this experiment, we simulate true surface fluxes of $7.14\ \mathrm{g\ m^{-2}\ s^{-1}}$, corresponding to a median enhancement level of 10 ppb. A summary of the prior parameters used in this single ensemble member inversion is detailed in Table 4. A metric of success is how well the inversion can correctly determine the true flux for pixels in emitting regions and identify zero-flux in the non-emitting regions.

Table 4: Experiment 1 parameters.

Region	Type	True Flux ($\mathrm{g\ m^{-2}\ s^{-1}}$)	Prior Flux Mean ($\mathrm{g\ m^{-2}\ s^{-1}}$)	Prior Uncertainty (%)
0–2	Emitting	7.14	5.36	100
3–7	Non-emitting	0	7.14×10^{-3}	200

2.5.2 Experiment 2: multi-ensemble member

In the second experiment, "multi-ensemble member", we examine how an ensemble of inversions further increases robustness of the estimate of the posterior flux estimates compared to truth. Ensembles are used to reduce the uncertainty around prescribing prior parameters. The true flux is the same as Experiment 1. We perform an ensemble of 36 inversions with prior parameters set as outlined in Table 3.

2.5.3 Experiment 3: flux magnitude sensitivity

In the third experiment, "flux magnitude sensitivity", we then investigate how flux retrievals using path-averaged laser beam concentration measurements behave across a range of true flux levels (7.14×10^{-2} to $7.14 \times 10^{4}\ \mathrm{g\ m^{-2}\ s^{-1}}$) resulting in a corresponding range of median enhancements (0.1 ppb to 1×10^{5} ppb). The full range of flux (and correspondingly, enhancement) levels are defined in Table 2.

https://doi.org/10.5194/egusphere-2026-3516
Preprint. Discussion started: 3 September 2026

2.5.4 Experiment 4: robustness to uncharacterized sources

Finally, in the fourth experiment, "robustness to uncharacterized sources", we examine how lack of knowledge of nearby confounding sources affects flux estimates. Again, when creating synthetic data, we impose a uniform flux rate for pixels within regions 0, 1, and 2; however, for this experiment’s prior, we only consider pixels in region 0 and 1 as source regions and all pixels in regions 2-7 non-source regions. As a result, the fluxes of pixels in region 2 will be dramatically underestimated by the prior. We assess our ability to still correctly retrieve the fluxes within regions 0 and 1, as well as our ability to overcome our incorrect prior assumption that pixels in region 2 are not emitting. We additionally assess how well our inversion correctly attributes zero flux to regions of non-emitting pixels. This experiment assesses flux retrievals across the same range of flux levels as Experiment 3.

2.6 Inversion assessment metrics

For each experiment, we compute the retrieved flux rate at each inversion pixel in the entire inversion domain. We then aggregate fluxes to compute average flux rate estimates for each region as defined in Fig. 1. For emitting regions (regions 0, 1, and 2), we compare the posterior flux value to the true flux value by calculating a percent error between the posterior flux values $\hat{\vec{x}}_{\text{flux}}$ aggregated over each emitting region r and the true flux level.

$$\text{Percent Error}_{r,\text{emitting}} = \frac{\hat{x}_{\text{flux},r} - x_{\text{flux},r}^{\text{true}}}{x_{\text{flux},r}^{\text{true}}} \times 100$$

For non-emitting regions (regions 3, 4, 5, 6, and 7), the above equation is undefined. To measure how well the inversion system correctly retrieved a zero flux, we utilize the true flux rate of the emitting regions to normalize the error for non-emitting regions.

$$\text{Percent Error}_{r,\text{non-emitting}} = \frac{\hat{x}_{\text{flux},r}}{x_{\text{flux}}^{\text{true}}} \times 100$$

This allows for easy comparison as we assess the inversions system’s performance across different magnitudes of true fluxes in experiments three and four.

3 Results and discussion

3.1 Experiment 1: single ensemble member

We calculate the solution to the Bayesian inverse problem by solving simultaneously for the scaling factors on the flux and background concentrations as defined in Section 2.1.

https://doi.org/10.5194/egusphere-2026-3516
Preprint. Discussion started: 3 September 2026

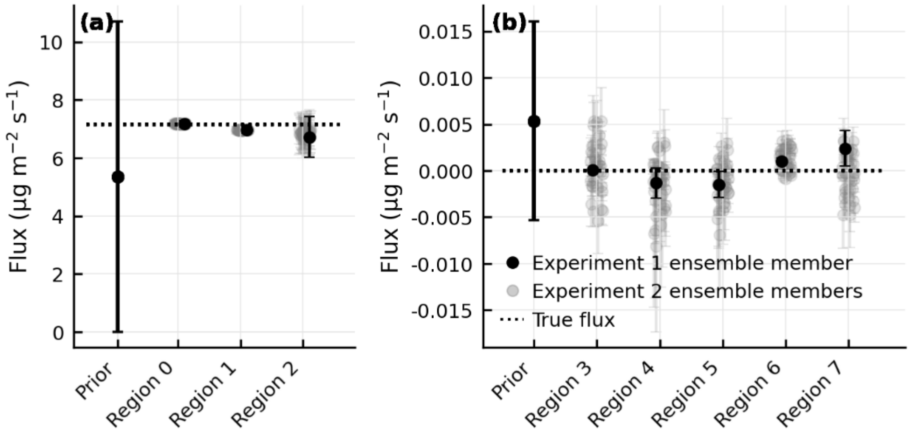

Figure 3: Aggregated prior, true, and posterior flux estimates for (a) emitting regions 0-2, and (b) and non-emitting regions 3-7. The horizontal green dotted line shows the true flux value. Black points show the single ensemble member's mean posterior, with uncertainty, from Experiment 1. Gray points show all ensemble member results for the same flux level (Experiment 2).

For a quantitative metric of how accurately the inversion can constrain fluxes over a region of interest, we compute the region-aggregated posterior flux estimates and their uncertainties. Figure 3 shows the results of this aggregation for the single inversion ensemble member used in Experiment 1 in black. Error bars represent the posterior's standard deviation after aggregation over each of the flux quantification regions. The mean-bias for a single inversion is small compared to the low-biased prior (for example, resulting mean-bias -5.9% of the true flux value for region 2 and -0.021% for region 5). Despite a biased prior flux in the source regions, the laser beam measurements provide observational constraint and reduce bias in the posterior estimate. The inversion successfully recovers fluxes in emitting regions while correctly identifying non-emitting regions.

3.1.1 Mean values

The results of the single inversion ensemble member are shown in Fig. 4. The top half of Fig. 4 shows the spatial distribution of the prior fluxes (a), the scaling factors on these priors retrieved by the inversion (b), and the corresponding posterior estimate of the fluxes (c). As described in Table 4, the prior estimate for the pixels in the source regions (0-2) was assigned lower-than-true value, and the prior for pixels in the non-source regions (3-7) were assigned higher-than-true value. The inversion adjusts each source type in the correct direction toward truth. The posterior fluxes within source regions are, on average, higher than the prior estimate (green) and the posterior flux estimates within non-source regions are lower than the prior estimate (blue).

https://doi.org/10.5194/egusphere-2026-3516
Preprint. Discussion started: 3 September 2026

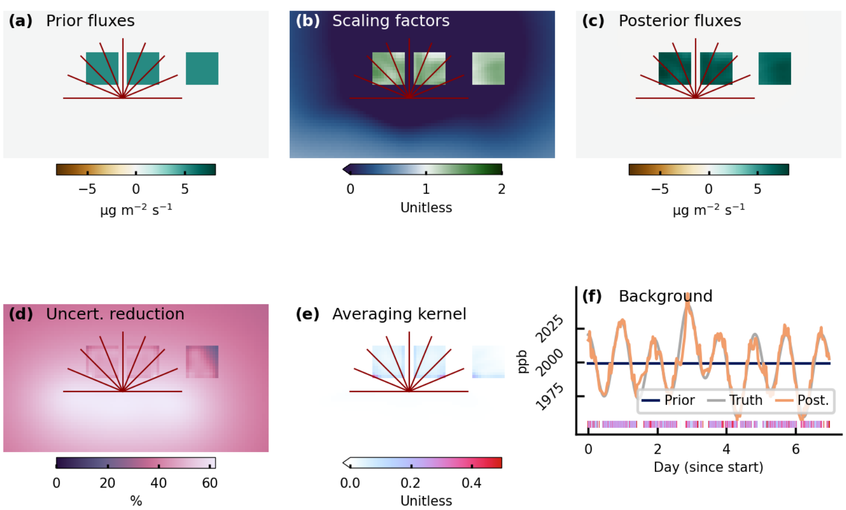

Figure 4: Results from a single inversion example. (a) Prior flux distribution. (b) Posterior scaling factors showing the ratio of posterior to prior estimates. (c) Posterior flux estimates. (d) Uncertainty reduction achieved by the inversion, expressed as a percentage. (e) Averaging kernel diagonal elements indicating the degree to which each pixel is constrained by the observations vs the prior estimate. (f) Background concentration timeseries showing prior, posterior, and true values, with colored bars at bottom indicating the averaging kernel values for background estimation (same color scale as (e)). An averaging kernel near unity indicates that this state vector element is constrained more by the observations than the prior estimate.

We observe spatial heterogeneity across the scaling factor map at finer spatial scales than the quantification regions. This is a feature of solving the inverse problem at a high spatial resolution and then aggregating flux estimates to our eight regions (0-7). Future work could assess flux heterogeneity with the same inversion modeling system and determine the smallest scale flux patterns that can be well-constrained by the measurements. Additionally, flux scaling factors illuminate the prior error covariance matrix's structure. We see low spatial frequency behavior in the posterior flux scaling factor across each region type (source and non-source) but we preserve a sharp cutoff between these regions. This reflects how the prior error covariance matrix structure may be leveraged to constrain the inversion solution.

3.1.2 Uncertainty estimates

Figure 4, panel (d) shows the uncertainty reduction provided by the inversion. We see that, in general, the observations have reduced the uncertainty in fluxes across the entire inversion domain. For the emitting regions, we see the highest uncertainty reduction within region 0 (57.4%). The lowest uncertainty reduction for an emitting region is at the far edge of region 2 (18.8%). Region 2 is the furthest from any measurement beam path, and the average laser beam footprint value drops with increasing distance from the laser beams (Fig. 1 (b)). For the same flux rate, enhancements due to a flux in region 2 are weaker than regions 0 and 1. With instrument-dominated observational error (as is the case in this experiment), enhancements due to region 2 yield lower signal-to-noise ratios than enhancements due to pixels which are closer to the instrument.

https://doi.org/10.5194/egusphere-2026-3516
Preprint. Discussion started: 3 September 2026

For the non-source regions, we see the largest uncertainty reduction to the South of the laser observing system (region 6: 62.2%) which is outside the laser beam fan. The use of real-world atmospheric data in our simulation results in a non-uniform wind direction distribution. In this dataset, most of the wind comes from the South (see Fig. 2). This setup mimics a system configuration in which the sensor is oriented to maximize "clean" background concentration measurements. A consequence of this setup is that we best constrain the fluxes outside of our primary area of interest (i.e., regions 0 and 1). We see corresponding wind direction-dependent uncertainty reduction in the posterior estimate of the background concentration (see Fig. S3).

The diagonal elements of the averaging kernel are plotted in panel (e) of Fig. 4. We compute the Degrees of Freedom for Signal (DOFS) for the flux pixels (20.3) and the DOFS for the background concentrations (80.4) (see Fig. S5). This represents the number of independent pieces of information that the inversion can constrain. We note that for this inversion, we do not have enough information to independently constrain each of the 4500 flux pixels, or 336 background concentration time points. We can aggregate the posterior fluxes to coarser spatial resolution where each aggregated region may be more independently constrained.

Despite accurate flux quantification, we see that the averaging kernel and uncertainty reduction indicate that the posterior flux estimate is not completely determined by the observations. Some constraint is still imposed by our flux prior (averaging kernel $\ll 1$). As a result, it is likely that our choices of prior error uncertainties affect the specific value of the posterior flux estimate. To address this uncertainty inherent to assigning prior fluxes, we analyze an ensemble of inversions with varying prior flux estimates and uncertainties in Section 3.2.

The posterior error correlation matrix ($\hat{\mathbf{S}}$ normalized by the square roots of its diagonal elements) characterizes how independently we can constrain the fluxes in each region with our observations. These statistics provide further insight when interpreting inversion results. Large values of posterior error correlation (i.e. near 100%) indicate that our estimates of corresponding regions are not *independently* constrained by our laser beam concentration observations. The full posterior error correlation for this inversion is shown in Fig. S4. The posterior correlations for this inversion suggest that we independently constrain each source region (i.e. region 0, 1, and 2: max absolute posterior error correlation -4.8% between regions 0 and 1). The highest absolute posterior error correlation is between regions 4 and 5 (75.7%), highlighting the high degree to which the inversion cannot independently constrain fluxes from these regions with the synthetic observations and corresponding uncertainties. We observe that regions 4 and 5 are situated primarily in the along-beam directions. Because the laser beams can only measure the path-averaged concentration, they are not necessarily able to provide much localization information, especially in the along-beam direction where the beams' concentration footprints do not exhibit strong variation across these regions. The posterior correlation matrix illuminates that we should not attempt to interpret the flux estimates from these regions in isolation, but may be able to further aggregate to a coarser scale including both regions.

https://doi.org/10.5194/egusphere-2026-3516
Preprint. Discussion started: 3 September 2026

3.1.3 Background concentration retrieval

Panel (f) shows the true, prior, and posterior pseudo-observations. Beginning with a constant-in-time prior background concentration (dark blue), the posterior background concentrations (orange) are able to correctly capture the oscillations in the background concentration time series (RMSE: 5.53 ppb; see Fig. 1). Panel (f) also shows the averaging kernel diagonal value for each time point (using the same color scale as panel (e)). We find that, in general, the averaging kernel values for the background concentrations are almost two orders of magnitude higher (mean 0.2393 for all background concentration averaging kernel averaged through time) compared to the flux averaging kernel values (mean 0.0045 across all flux pixels in space), indicating that the data provide a much better constraint on the background concentrations than on the fluxes. For Experiment 1, the reasons the background concentrations are better-constrained than the fluxes are threefold. Firstly, the pseudodata are dominated by contributions from the background (mean 2000 ppb) over the enhancements (median 10 ppb for Beam 3 and lower for all others). Additionally, the inversion system takes into account the contribution of measurement and transport model error when mapping fluxes to enhancements; however, the assumption that all laser beams measure the same, spatially uniform background concentration is not subject to any model error. Finally, during each individual measurement period, only a portion of the domain is sampled by the laser beam footprints. In contrast, the background concentration is measured at all time points, receiving constraint from the laser beam measurements. For these reasons, we might expect that the background concentrations contain more constraint from the measurements, as indicated by the higher DOFS and averaging kernel values.

3.2 Experiment 2: multi-ensemble member

To assess robustness of the inversion result to uncertainty in the mean of the prior flux estimate, we repeat the inversion calculations for each of the 36 inversion ensemble members. The true flux is the same as Experiment 1. Analysis of all 36 ensemble members reveals robust flux retrievals, despite significant uncertainty in prior means and an imperfect dispersion model (Fig. 3). For each ensemble member, we compute the posterior flux aggregated over each region. In practice, inversion ensembles would be used to post-process a single set of measurements to isolate the effect of inversion input parameters. To mimic this behavior, the synthetic observations used in each inversion ensemble are generated using the same realization of observational error. The result is an equally valid ensemble of flux estimates. We then compute the ensemble estimate of the flux by taking the mean of each ensemble's flux estimate values. We capture the spread of the ensemble with the standard deviation of the ensemble members' estimates. This spread helps quantify the inversion sensitivity to reasonable prior assumptions.

The spread in the posterior flux values in Fig. 3 shows the importance of using an inversion ensemble to avoid over-reliance on the results of a single choice of prior flux. While an individual ensemble member may not include the true flux value, the spread of all ensemble members better capture the true flux. The ensemble mean estimate reduces the mean flux bias compared to a single ensemble member. For example, in the inversion shown in Fig. 3, region 2's ensemble estimate mean

https://doi.org/10.5194/egusphere-2026-3516
Preprint. Discussion started: 3 September 2026

bias is reduced to -4.3% compared with -5.9% for the estimate from the single ensemble member described in Section 3.1. For region 5, the full ensemble estimate's mean-bias is reduced to -0.017% compared with that same individual ensemble member's estimate of -0.021%. We see that, even for cases where a single inversion member may produce a biased emission estimate, the ensemble increases robustness in the inversion system and improves our ability to retrieve the true mean.

3.3 Experiment 3: flux magnitude sensitivity

We have seen that our inversion system accurately retrieves the week-averaged emissions while simultaneously retrieving a background concentration. We now explore how this performance scales over a range of true flux values (and therefore atmospheric concentration enhancements). For each true flux rate, we conduct an ensemble of inversions where prior flux magnitudes and uncertainties are assigned relative to the true flux as defined in Table 3. For each flux level, we calculate the region-aggregated posterior estimate of the flux and the averaging kernel matrix diagonal for regions (0-7). Results of inversion ensembles across the range of true fluxes are shown in Fig. 5. We calculate the mean of the posterior flux estimates across all ensemble members. We capture the spread in flux and averaging kernel diagonal due to different ensemble members with the standard deviation of the mean values from each of the 36 ensemble members.

https://doi.org/10.5194/egusphere-2026-3516
Preprint. Discussion started: 3 September 2026

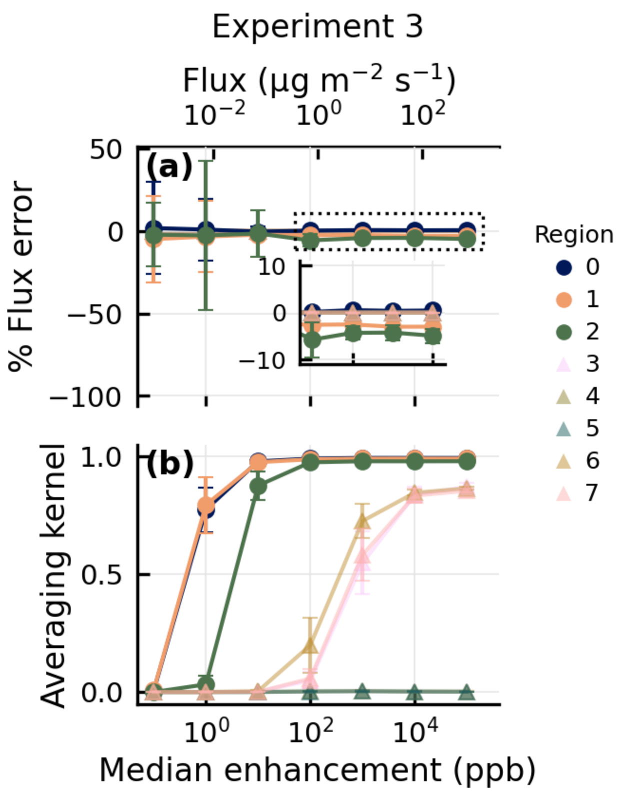

Figure 5: Ensemble flux estimation performance with all emitting regions included in the prior for different median enhancement values. (a) Percent flux error as a function of median enhancement level and true underlying flux. Bars show ensemble standard deviation. Colors correspond to regions as defined in Fig.1 Emitting regions (0-2) are shown in solid colors with circle markers and non-emitting regions (3-7) are shown transparently with triangle markers to aid in interpretation. (b) Averaging kernel values aggregated for each region, indicating the degree to which each region's ensemble estimate of the flux is constrained by observations. Higher flux (and therefore enhancement levels) lead to reduced flux errors and averaging kernels approaching unity, indicating well-constrained estimates.

At the lowest true flux and enhancement level (7.14×10^{-2} g m^{-2} s^{-1}, corresponding to 0.1 ppb median enhancement), our flux estimates default to the prior flux. The averaging kernel for all flux regions is less than 0.01, suggesting that virtually no information is provided by the measurements for this flux rate. At the second lowest flux level (7.14×10^{-1} g m^{-2} s^{-1}, corresponding to 1 ppb median enhancement), we are able to constrain the fluxes in regions 0 and 1 with one week of laser beam measurements, even in the presence of simultaneously retrieving an unknown background concentration (range of averaging kernel 0.57- 0.90 and 0.51-0.91 for regions 0 and 1, respectively). The error bars on our flux estimates for regions 0 and 1 begin to narrow relative to the prior but still exhibit some spread. Region 2, being far from the measurement locations, receives incomplete constraint by the measurements (aggregated averaging kernel: 0.026). The mean inversion estimate for region 2 is near zero error (mean: -2.71%), however individual ensemble estimates show large variability (standard deviation: 45.05%). The aggregated averaging kernel (0.026) helps contextualize that these estimates are hardly constrained by our measurements. The posterior estimate is highly sensitive to the prior estimates and uncertainty choices of each inversion ensemble member. For both of these flux cases, the observational error is dominated by instrument

https://doi.org/10.5194/egusphere-2026-3516
Preprint. Discussion started: 3 September 2026

noise (Fig. 3). Larger flux values result in proportionally larger enhancements for the same instrument noise. The result is that larger fluxes are better constrained when the observational error is instrument-noise dominated. The averaging kernel, relative observational error contributions, and large ensemble spread helps contextualize our overall low confidence in region 2 flux estimates when per-beam median concentrations are at or less 1 ppb. Applying Bayesian statistical treatment of the inversion problem adds additional metrics to contextualize the interpretation of our inversion results.

At flux values of $7.14\ \mathrm{g\ m^{-2}\ s^{-1}}$ (median enhancement 100 ppb) and greater, all source regions are well-constrained by the measurements (minimum aggregated averaging kernel >= 0.98). The posterior estimate shows low sensitivity to prior assumptions, indicated by narrow ensemble spreads (0.63%: region 0, 0.53%: region 1, 3.05%: region 2). The ensemble's mean posterior estimates asymptote to stable values near zero error, but exhibit small, but persistent mean-bias. For the highest true flux level, ensemble mean accuracies are 0.45%, -2.98% -4.79% for source regions 0, 1, and 2 respectively (see Fig. 5, panel (a) inset).

This stable bias is likely due to our assumption of proportional transport model error and the underlying distribution of observational error. The Bayesian inversion framework assumes that all uncertainties are normally distributed and can be described with their first two statistical moments. Because of how we've constructed transport model error, the transport model component of observational error will have a distribution which follows that of the enhancements due to the true underlying flux, $\vec{z}_{\mathrm{enhancement}}$. It is quite likely that enhancement data do not follow a Gaussian distribution (skewness=1.7). This mismatch in Gaussian assumption and actual enhancement distribution may lead to the stable bias observed in the ensemble-retrieved fluxes, even as concentration signals grow large compared to instrument error and background concentration. For fluxes $7.14 \times 10^{1}\ \mathrm{g\ m^{-2}\ s^{-1}}$ and greater, transport model error (which is proportional to enhancement and therefore flux strength) is the dominant contribution to our observational error (Fig. 3). Even as fluxes increase, the dominant observational error source increases proportionally, explaining the stability of the bias across flux levels.

Flux retrievals demonstrate accuracy, even in the presence of instrument and transport model error. Future work could explore the use of assuming log-normal statistics in the inversion setup (Cui et al. 2019). With sufficient enhancement signal, we can accumulate many laser beam measurements to accurately infer a week-averaged emission rate. The inversion system produces estimates with high accuracy relative to a dispersion model, which may only be $\pm 20\%$ accurate.

3.4 Experiment 4: robustness to uncharacterized source

We repeat the flux magnitude analysis in Experiment 3, but with region 2 excluded from the prior. This experiment is designed to test robustness of our inversion results to the existence of a source that may not be know *a prior*. In this experiment, when the measurements provide ample constraint on the fluxes (i.e., averaging kernel near 1), the inversion system still retrieves flux rates with reasonable accuracy for the regions within the fan of the laser beams (max absolute error of -4.53%: region 0 and 6.86%: region 1 when aggregated averaging kernel values > 0.95). For regions 0 and 1, we see a similar pattern of constraint provided by the data as a function of flux level as with Experiment 3; however, the use of an imperfect prior (missing hypothesized emission in region 2) introduces more variability in the posterior estimates. At flux

https://doi.org/10.5194/egusphere-2026-3516
Preprint. Discussion started: 3 September 2026

values of 7.14 $g \ m^{-2} \ s^{-1}$ (median enhancement 100 ppb) and greater, the averaging kernel for regions 0 and 1 asymptotes near 1, however flux estimates across all regions diverge from zero with increasing flux strength (see Fig. 6, panel (a) inset). With a local emission source not accounted for in the prior flux estimate, the inversion is more sensitive overall to the prior
585 estimate, but the flux estimates remain accurate within the 20% uncertainty in the dispersion model.

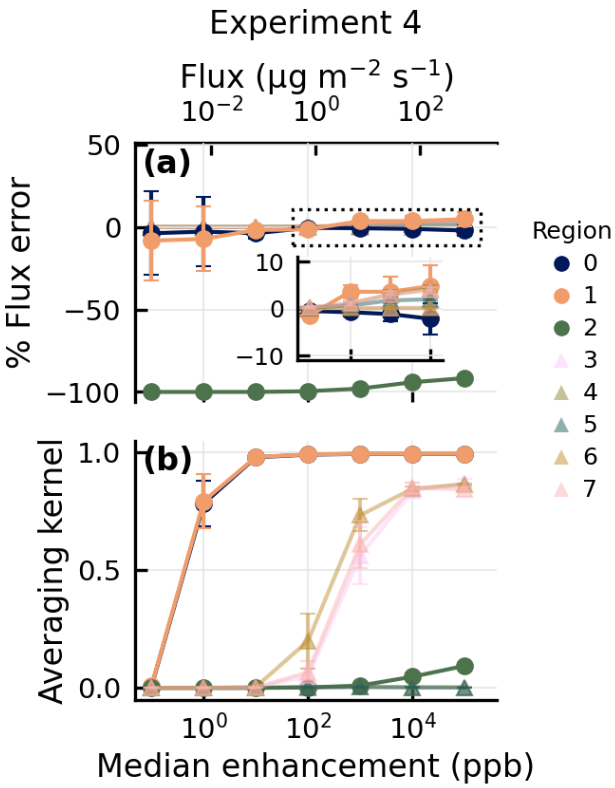

Figure 6: Ensemble flux estimation performance with pixels in region 2 considered non-source regions in the prior. Panel layout follows the same convention as Fig 5. This configuration tests the inversion's ability to estimate fluxes when one source region is not included in the prior, representing a scenario where the existence of nonzero emissions might be unknown or incorrectly specified.

590 The posterior flux estimate for region 2 demonstrate large errors due to the strongly incorrect prior flux estimate. The spread of the posterior estimates for region 2 depart from zero (-100%) for fluxes with median enhancements of 100 ppb and higher (mean error -99.58% $\pm$ 0.27%, averaging kernel 0.0017). As enhancements increase, the inversion begins to more correctly attribute flux to this region, despite a prior estimate that suggested no emission was present in Region 2.

An interesting artifact of this form of inaccuracy in the prior flux estimate is that the non-emitting regions also begin to
595 retrieve non-zero flux estimates. This increase in flux attributed to all non-source regions (not just region 2) may be due, in part, to the spatial correlation imposed in the flux uncertainties, $\mathbf{S}_a$, across all pixels designated as non-source. We assume that errors in our prior flux estimate are spatially correlated to encode the assumption that our uncertainty in the fluxes of are spatially correlated for diffuse fluxes. A side effect of this assumption may therefore be that if the prior flux distribution is mis-specified, the constraint imposed by the prior error covariance matrix may result in attributing fluxes to a broader spatial

https://doi.org/10.5194/egusphere-2026-3516
Preprint. Discussion started: 3 September 2026

area (consistent with the assumption encoded in $\mathbf{S}_a$), even when the emission originates from a more spatially discrete location. This highlights the importance of prescribing prior error covariance parameters for local-scale quantification. Future work could assess the effect of spatial correlation on inversion outputs, both in simulation and for real-world deployments. Accuracy in background estimation between experiments 3 and 4 further highlights how the uncharacterized source affects the inversion result. We calculate the root mean squared error (RMSE) for the background concentration timeseries. At low flux values, background RMSE are small for both experiment 3 (min value 2.01 ± 0.65 ppb) and experiment 4 (min value 2.01 ± 0.59 ppb). In experiment 3, background RMSE remains near or below the 7 ppb instrument error (max value 7.58 ± 2.83 ppb) across true flux values. In experiment 4, when we have an uncharacterized source in the prior, determination of background concentration suffers as flux increases (max background concentration RMSE 80.24 ± 46.37 ppb). Additionally, for experiment 4, the background RMSE ensemble spread increases with increasing flux levels. The full behavior of background RMSE for experiments 3 and 4 is shown in Fig. 7.

With an imperfect prior flux distribution assumption, we task the inversion to attribute fluxes and background concentrations consistent with the prior, prior error covariance, and the observations. Both flux and background retrieval errors are symptoms of the inability of the inversion to reconcile observations with an imperfect prior. The bias in the prior (i.e., missing the existence of emission from pixels within region 2) leads to a bias in the posterior estimate of flux and the retrieved background concentration. The maximum background RMSE values may be large compared to the 20 ppb background variation; however, at the highest flux levels, the mean background RMSE is quite small relative to the median enhancements (0.08%) and the inversion still retrieves average fluxes in all regions within 10% - except region 2.

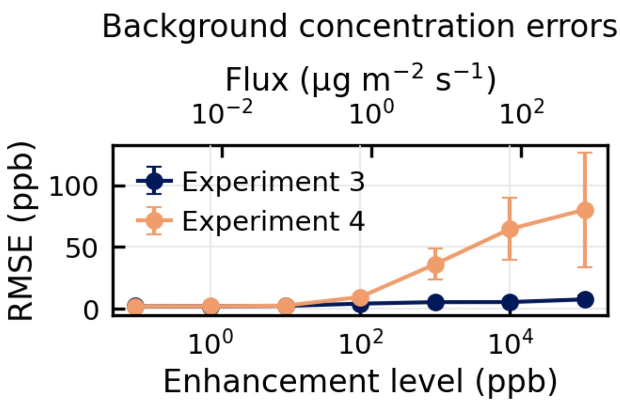

Figure 7: RMSE of background concentration estimates as a function of source strength and median enhancement level.

4 Conclusions

We find that the analytical Bayesian framework accurately retrieves diffuse surface-to-atmosphere fluxes, even in the presence of a time-varying background concentration. Including time-varying background concentrations in the state vector enabled this innovation. We accurately quantify near-to-beam area-source emissions when median enhancements are as low as 1 ppb by leveraging one week of (n=3024) path-averaged laser beam concentration measurements.

https://doi.org/10.5194/egusphere-2026-3516
Preprint. Discussion started: 3 September 2026

When the prior flux estimates accurately capture fluxes heterogeneity, and more specifically that non-source and source areas are correctly categorized in the a priori estimates, the posterior flux estimates demonstrate high accuracy across true flux levels. Small (<10%), stable biases arise despite large enhancement-to-instrument-error ratios (Section 3.3), due to our assumption of the proportional nature of transport model error.

At higher true flux values (and consequently higher atmospheric concentration enhancements), transport model error dominates the observational error budget. The proportional nature of transport model error leads to a mismatch between the underlying assumption of Gaussianity in the Bayesian framework and the actual distribution of the concentration measurements. When the prior flux distribution excludes a nearby source that exists in "reality" (Section 3.4), flux and background concentration quantification remains robust to this uncertainty. With larger true fluxes, quantification performance degrades and aggregated flux estimate error departs from zero, further highlighting the impact of transport-dominated observational error. Regardless of prior flux assumptions, inversion solution flux estimates remain accurate within the transport model uncertainty (20% in this study).

We acknowledge that the Backward Lagrangian Stochastic (BLS) model used in this study relies on simplified parameterizations of flow in the atmospheric boundary layer. Future studies could leverage higher fidelity atmospheric transport models (e.g. Gaussian Puff (Jia et al. 2025) or Reynolds Averaged Navier Stokes (Berchet et al. 2017) which can resolve flow heterogeneity and potentially model the effect of terrain. These more advanced models may reduce the uncertainty in the inversion due to the transport model, which dominates at high fluxes and measured enhancement. We base this work on a high-precision (7 ppb) path-averaged concentration sensor (Section 2.3.5). Future work could assess the ability of lower-precision instruments to infer fluxes with the Bayesian framework especially at high flux levels when instrument error is dwarfed by transport model error. Treating the instrument and transport model together in the Bayesian framework allows for prioritization of uncertainty reduction based on the relative contributions of instrument and transport model for a given enhancement.

This OSSE framework presents an opportunity to simulate open-path laser-beam system configurations before real-world deployments. Future work could employ this framework to optimize the laser beam geometry given representative meteorological data and prior flux assumptions. By employing an end-to-end simulation of the observing system (i.e. laser system and transport model) and its errors (i.e. instrument, atmospheric transport, and prior), once could optimize beam geometry to maximize independent constraint of fluxes at specific locations.

Code and data availability

The code used in this study is not publicly available due to intellectual property and commercial considerations related to ongoing licensing activities.

https://doi.org/10.5194/egusphere-2026-3516
Preprint. Discussion started: 3 September 2026

Author contributions

EAM, GBR, SC, and CA conceptualized the study. EAM developed the methodology and software, performed all formal analysis and investigation, and wrote the original draft. GBR, CA, and TRJ acquired funding. DH and CA contributed to methodology. All authors contributed to review and editing of the manuscript. GBR provided project oversight.

Competing interests

Authors GBR, CA, and SC have a financial interest in LongPath Technologies, Inc.

Acknowledgements

This work utilized the Alpine High-Performance Computing resource at the University of Colorado Boulder. Alpine is jointly funded by the University of Colorado Boulder, the University of Colorado Anschutz, Colorado State University, and the National Science Foundation (award 2201538)

References

Alden, Caroline B., Sean C. Coburn, Robert J. Wright, et al. 2019. "Single-Blind Quantification of Natural Gas Leaks from 1 Km Distance Using Frequency Combs." *Environmental Science & Technology* 53 (5): 2908–17. https://doi.org/10.1021/acs.est.8b06259.

Alden, Caroline B., Robbie J. Wright, Sean C. Coburn, et al. 2020. "Temporal Variability of Emissions Revealed by Continuous, Long-Term Monitoring of an Underground Natural Gas Storage Facility." *Environmental Science & Technology* 54 (22): 14589–97. https://doi.org/10.1021/acs.est.0c03175.

Aubinet, Marc, Timo Vesala, and Dario Papale, eds. 2012. *Eddy Covariance: A Practical Guide to Measurement and Data Analysis*. Springer Netherlands. https://doi.org/10.1007/978-94-007-2351-1.

Berchet, Antoine, Katrin Zink, Clive Muller, et al. 2017. "A Cost-Effective Method for Simulating City-Wide Air Flow and Pollutant Dispersion at Building Resolving Scale." *Atmospheric Environment* 158 (June): 181–96. https://doi.org/10.1016/j.atmosenv.2017.03.030.

Bousserez, N., and Daven K. Henze. 2018. "Optimal and Scalable Methods to Approximate the Solutions of Large-Scale Bayesian Problems: Theory and Application to Atmospheric Inversion and Data Assimilation." *Quarterly Journal of the Royal Meteorological Society* 144 (711): 365–90. https://doi.org/10.1002/qj.3209.

Brasseur, Guy, and Daniel J. Jacob. 2017. *Modeling of Atmospheric Chemistry*. Cambridge University Press.

Caulton, Dana R., Qi Li, Elie Bou-Zeid, et al. 2018. "Quantifying Uncertainties from Mobile-Laboratory-Derived Emissions of Well Pads Using Inverse Gaussian Methods." *Atmospheric Chemistry and Physics* 18 (20): 15145–68. https://doi.org/10.5194/acp-18-15145-2018.

Coburn, Sean, Caroline B. Alden, Robert Wright, et al. 2018. "Regional Trace-Gas Source Attribution Using a Field-Deployed Dual Frequency Comb Spectrometer." *Optica* 5 (4): 320–27. https://doi.org/10.1364/OPTICA.5.000320.

Crenna, B. P., T. K. Flesch, and J. D. Wilson. 2008. "Influence of Source–Sensor Geometry on Multi-Source Emission Rate Estimates." *Atmospheric Environment* 42 (32): 7373–83. https://doi.org/10.1016/j.atmosenv.2008.06.019.

Cui, Yu Yan, Daven K. Henze, Jerome Brioude, et al. 2019. "Inversion Estimates of Lognormally Distributed Methane Emission Rates From the Haynesville-Bossier Oil and Gas Production Region Using Airborne Measurements." *Journal of Geophysical Research: Atmospheres* 124 (6): 3520–31. https://doi.org/10.1029/2018JD029489.

Dogniaux, Matthieu, Joannes D. Maasakkers, Marianne Girard, et al. 2025. "Global Satellite Survey Reveals Uncertainty in Landfill Methane Emissions." *Nature*, ahead of print, November. https://doi.org/10.1038/s41586-025-09683-8.

Elder, C. D., D. R. Thompson, A. K. Thorpe, et al. 2021. "Characterizing Methane Emission Hotspots From Thawing Permafrost." *Global Biogeochemical Cycles* 35 (12): e2020GB006922. https://doi.org/10.1029/2020GB006922.

Fan, Jianqing, and James S. Marron. 1994. "Fast Implementations of Nonparametric Curve Estimators." *Journal of Computational and Graphical Statistics* 3 (1): 35–56. https://doi.org/10.1080/10618600.1994.10474629.

Flesch, T. K., J. D. Wilson, L. A. Harper, B. P. Crenna, and R. R. Sharpe. 2004. "Deducing Ground-to-Air Emissions from Observed Trace Gas Concentrations: A Field Trial." *Journal of Applied Meteorology* 43 (3): 487–502. https://doi.org/10.1175/1520-0450(2004)043<0487:dgefot>2.0.co;2.

Flesch, T., V. Baron, John D. Wilson, D. Griffith, J. Basarab, and P. J. Carlson. 2016. *Agricultural Gas Emissions During the Spring Thaw: Applying a New Measurement Technique*. https://doi.org/10.1016/J.AGRFORMET.2016.02.010.

Flesch, Thomas K., Lowry A. Harper, Trevor W. Coates, and Peter J. Carlson. 2023. "Estimation of Gas Emissions from a Waste Pond Using Micrometeorological Approaches: Footprint Sensitivities and Complications." *Atmospheric Environment: X* 19 (August): 100219. https://doi.org/10.1016/j.aeaoa.2023.100219.

Flesch, Thomas K., Lowry A. Harper, Raymond L. Desjardins, Zhiling Gao, and Brian P. Crenna. 2009. "Multi-Source Emission Determination Using an Inverse-Dispersion Technique." *Boundary-Layer Meteorology* 132 (1): 11–30. https://doi.org/10.1007/s10546-009-9387-1.

Flesch, Thomas K., John D. Wilson, and Eugene Yee. 1995. "Backward-Time Lagrangian Stochastic Dispersion Models and Their Application to Estimate Gaseous Emissions." *Journal of Applied Meteorology and Climatology* 34 (6): 1320–32. https://doi.org/10.1175/1520-0450(1995)034<1320:BTLSDM>2.0.CO;2.

Flesch, T, J Wilson, L Harper, and B Crenna. 2005. "Estimating Gas Emissions from a Farm with an Inverse-Dispersion Technique." *Atmospheric Environment* 39 (27): 4863–74. https://doi.org/10.1016/j.atmosenv.2005.04.032.

Fukunaga, Keinosuke. 2009. *Introduction to Statistical Pattern Recognition*. 2. ed., [reprint]. Computer Science and Scientific Computing. Academic Press.

Haan, Peter De. 1999. "On the Use of Density Kernels for Concentration Estimations Within Particle and Puff Dispersion Models." *Atmospheric Environment* 33 (13): 2007–21. https://doi.org/10.1016/S1352-2310(98)00424-5.

Han, Jin-Jian, Wei Zhong, Ruo-Can Zhao, et al. 2024. "Dual-Comb Spectroscopy over a 100 Km Open-Air Path." *Nature Photonics* 18 (11): 1195–202. https://doi.org/10.1038/s41566-024-01525-9.

Hashemi, Josh, Aleksi Räsänen, Tarmo Virtanen, et al. 2025. "Coarse Land Cover Datasets Bias Arctic-Boreal Wetland Methane Budgets." *Communications Earth & Environment* 6 (1): 903. https://doi.org/10.1038/s43247-025-02963-1.

Herman, Daniel I., Chinthaka Weerasekara, Lindsay C. Hutcherson, et al. 2021. "Precise Multispecies Agricultural Gas Flux Determined Using Broadband Open-Path Dual-Comb Spectroscopy." *Science Advances* 7 (14): eabe9765. https://doi.org/10.1126/sciadv.abe9765.

Hirst, Bill, David Randell, Matthew Jones, et al. 2020. "Methane Emissions: Remote Mapping and Source Quantification Using an Open-Path Laser Dispersion Spectrometer." *Geophysical Research Letters* 47 (10): e2019GL086725. https://doi.org/10.1029/2019GL086725.

Hu, Enzhu, Esther L. Babcock, Stephen E. Bialkowski, Scott B. Jones, and Markus Tuller. 2014. "Methods and Techniques for Measuring Gas Emissions from Agricultural and Animal Feeding Operations." *Critical Reviews in Analytical Chemistry* 44 (3): 200–219. https://doi.org/10.1080/10408347.2013.843055.

Hugelius, G., J. Ramage, E. Burke, et al. 2024. "Permafrost Region Greenhouse Gas Budgets Suggest a Weak CO_2 Sink and CH_4 and N_2 O Sources, But Magnitudes Differ Between Top-Down and Bottom-Up Methods." *Global Biogeochemical Cycles* 38 (10): e2023GB007969. https://doi.org/10.1029/2023GB007969.

IJzermans, Rutger, Matthew Jones, Damien Weidmann, Bas Van De Kerkhof, and David Randell. 2024. "Long-Term Continuous Monitoring of Methane Emissions at an Oil and Gas Facility Using a Multi-Open-Path Laser Dispersion Spectrometer." *Scientific Reports* 14 (1): 623. https://doi.org/10.1038/s41598-023-50081-9.

Intergovernmental Panel On Climate Change (Ipcc). 2023. *Climate Change 2021 – The Physical Science Basis: Working Group I Contribution to the Sixth Assessment Report of the Intergovernmental Panel on Climate Change*. 1st ed. Cambridge University Press. https://doi.org/10.1017/9781009157896.

Jacob, Daniel J., Alexander J. Turner, Joannes D. Maasakkers, et al. 2016. "Satellite Observations of Atmospheric Methane and Their Value for Quantifying Methane Emissions." *Atmospheric Chemistry and Physics* 16 (22): 14371–96. https://doi.org/10.5194/acp-16-14371-2016.

Jacob, Daniel J., Daniel J. Varon, Daniel H. Cusworth, et al. 2022. "Quantifying Methane Emissions from the Global Scale down to Point Sources Using Satellite Observations of Atmospheric Methane." *Atmospheric Chemistry and Physics* 22 (14): 9617–46. https://doi.org/10.5194/acp-22-9617-2022.

Jia, Meng, Ryker Fish, William S. Daniels, Brennan Sprinkle, and Dorit Hammerling. 2025. "A Fast and Lightweight Implementation of the Gaussian Puff Model for Near-Field Atmospheric Transport of Trace Gasses." *Scientific Reports* 15 (1): 18710. https://doi.org/10.1038/s41598-025-99491-x.

https://doi.org/10.5194/egusphere-2026-3516
Preprint. Discussion started: 3 September 2026

Johnson, Matthew R., Bradley M. Conrad, and David R. Tyner. 2023. "Creating Measurement-Based Oil and Gas Sector Methane Inventories Using Source-Resolved Aerial Surveys." *Communications Earth & Environment* 4 (1): 139. https://doi.org/10.1038/s43247-023-00769-7.

K. Patra, Prabir, Masayuki Takigawa, Kentaro Ishijima, et al. 2009. "Growth Rate, Seasonal, Synoptic, Diurnal Variations and Budget of Methane in the Lower Atmosphere." *Journal of the Meteorological Society of Japan. Ser. II* 87 (4): 635–63. https://doi.org/10.2151/jmsj.87.635.

Karacan, C. Özgen, Robert A. Field, Maria Olczak, Malgorzata Kasprzak, Felicia A. Ruiz, and Stefan Schwietzke. 2024. "Mitigating Climate Change by Abating Coal Mine Methane: A Critical Review of Status and Opportunities." *International Journal of Coal Geology* 295 (December): 104623. https://doi.org/10.1016/j.coal.2024.104623.

Kljun, N., M. W. Rotach, and H. P. Schmid. 2002. "A Three-Dimensional Backward Lagrangian Footprint Model For A Wide Range Of Boundary-Layer Stratifications." *Boundary-Layer Meteorology* 103 (2): 205–26. https://doi.org/10.1023/A:1014556300021.

Kohnert, Katrin, Bennet Juhls, Sina Muster, et al. 2018. "Toward Understanding the Contribution of Waterbodies to the Methane Emissions of a Permafrost Landscape on a Regional Scale—A Case Study from the Mackenzie Delta, Canada." *Global Change Biology* 24 (9): 3976–89. https://doi.org/10.1111/gcb.14289.

Kuhn, McKenzie A., Ruth K. Varner, David Bastviken, et al. 2021. "BAWLD-CH₄: A Comprehensive Dataset of Methane Fluxes from Boreal and Arctic Ecosystems." *Earth System Science Data* 13 (11): 5151–89. https://doi.org/10.5194/essd-13-5151-2021.

Metya, Abirlal, Amey Datye, Supriyo Chakraborty, et al. 2021. "Diurnal and Seasonal Variability of CO2 and CH4 Concentration in a Semi-Urban Environment of Western India." *Scientific Reports* 11 (1): 2931. https://doi.org/10.1038/s41598-021-82321-1.

Michalak, Anna M., Adam Hirsch, Lori Bruhwiler, Kevin R. Gurney, Wouter Peters, and Pieter P. Tans. 2005. "Maximum Likelihood Estimation of Covariance Parameters for Bayesian Atmospheric Trace Gas Surface Flux Inversions." *Journal of Geophysical Research: Atmospheres* 110 (D24): 2005JD005970. https://doi.org/10.1029/2005JD005970.

Miller, Scot M., Arvind K. Saibaba, Michael E. Trudeau, Marikate E. Mountain, and Arlyn E. Andrews. 2020. "Geostatistical Inverse Modeling with Very Large Datasets: An Example from the Orbiting Carbon Observatory 2 (OCO-2) Satellite." *Geoscientific Model Development* 13 (3): 1771–85. https://doi.org/10.5194/gmd-13-1771-2020.

Mønster, Jacob, Peter Kjeldsen, and Charlotte Scheutz. 2019. "Methodologies for Measuring Fugitive Methane Emissions from Landfills – A Review." *Waste Management* 87 (March): 835–59. https://doi.org/10.1016/j.wasman.2018.12.047.

Nesser, Hannah, Daniel J. Jacob, Joannes D. Maasakkers, et al. 2024. "High-Resolution US Methane Emissions Inferred from an Inversion of 2019 TROPOMI Satellite Data: Contributions from Individual States, Urban Areas, and Landfills." *Atmospheric Chemistry and Physics* 24 (8): 5069–91. https://doi.org/10.5194/acp-24-5069-2024.

https://doi.org/10.5194/egusphere-2026-3516
Preprint. Discussion started: 3 September 2026

Nikodem, Michal, Genevieve Plant, David Sonnenfroh, and Gerard Wysocki. 2015. "Open-Path Sensor for Atmospheric Methane Based on Chirped Laser Dispersion Spectroscopy." *Applied Physics B* 119 (1): 3–9. https://doi.org/10.1007/s00340-014-5938-3.

Ocko, Ilissa B, Tianyi Sun, Drew Shindell, et al. 2021. "Acting Rapidly to Deploy Readily Available Methane Mitigation Measures by Sector Can Immediately Slow Global Warming." *Environmental Research Letters* 16 (5): 054042. https://doi.org/10.1088/1748-9326/abf9c8.

Odland, Tommy. 2018. *Tommyod/KDEpy: Kernel Density Estimation in Python*. Zenodo. https://doi.org/10.5281/ZENODO.2392268.

Padilla, R., J. A. Adame, P. J. Hidalgo, J. P. Bolivar, and M. Yela. 2024. "Short-Term Trend and Temporal Variations in Atmospheric Methane at an Atlantic Coastal Site in Southwestern Europe." *Atmospheric Environment* 333 (September): 120665. https://doi.org/10.1016/j.atmosenv.2024.120665.

Pallandt, Martijn M. T. A., Abhishek Chatterjee, Lesley E. Ott, Julia Marshall, and Mathias Göckede. 2025. "If the Yedoma Thaws, Will We Notice? Quantifying Detection Limits of Top-down Methane Monitoring Infrastructures." *Atmospheric Measurement Techniques* 18 (22): 7053–73. https://doi.org/10.5194/amt-18-7053-2025.

Pernini, Timothy G., T. Scott Zaccheo, Jeremy Dobler, and Nathan Blume. 2022. "Estimating Oil Sands Emissions Using Horizontal Path-Integrated Column Measurements." *Atmospheric Measurement Techniques* 15 (2): 225–40. https://doi.org/10.5194/amt-15-225-2022.

Qian, Haoyu, Xiangchen Zhu, Shan Huang, et al. 2023. "Greenhouse Gas Emissions and Mitigation in Rice Agriculture." *Nature Reviews Earth & Environment* 4 (10): 716–32. https://doi.org/10.1038/s43017-023-00482-1.

Rieker, G. B., F. R. Giorgetta, W. C. Swann, et al. 2014. "Frequency-Comb-Based Remote Sensing of Greenhouse Gases over Kilometer Air Paths." *Optica* 1 (5): 290. https://doi.org/10.1364/OPTICA.1.000290.

Rodgers, Clive D. 2000. *Inverse Methods for Atmospheric Sounding: Theory and Practice*. Series on Atmospheric, Oceanic and Planetary Physics, v.2. World Scientific Pub. Co.

Rosentreter, Judith A., Alberto V. Borges, Bridget R. Deemer, et al. 2021. "Half of Global Methane Emissions Come from Highly Variable Aquatic Ecosystem Sources." *Nature Geoscience* 14 (4): 225–30. https://doi.org/10.1038/s41561-021-00715-2.

Saunois, Marielle, Adrien Martinez, Benjamin Poulter, et al. 2025. "Global Methane Budget 2000–2020." *Earth System Science Data* 17 (5): 1873–958. https://doi.org/10.5194/essd-17-1873-2025.

Schmitt, Tobias D., Jonas Kuhn, Ralph Kleinschek, et al. 2023. "An Open-Path Observatory for Greenhouse Gases Based on Near-Infrared Fourier Transform Spectroscopy." *Atmospheric Measurement Techniques* 16 (24): 6097–110. https://doi.org/10.5194/amt-16-6097-2023.

Silverman, B. W. 1998. *Density Estimation for Statistics and Data Analysis*. Monographs on Statistics and Applied Probability 26. Chapman & Hall/CRC.

https://doi.org/10.5194/egusphere-2026-3516
Preprint. Discussion started: 3 September 2026

Tagliaferri, Francesca, Marzio Invernizzi, Federica Capra, and Selena Sironi. 2023. "Validation Study of WindTrax Reverse Dispersion Model Coupled with a Sensitivity Analysis of Model-Specific Settings." *Environmental Research* 222 (April): 115401. https://doi.org/10.1016/j.envres.2023.115401.

Thoma, Eben D., Richard C. Shores, Edgar L. Thompson, et al. 2005. "Open-Path Tunable Diode Laser Absorption Spectroscopy for Acquisition of Fugitive Emission Flux Data." *Journal of the Air & Waste Management Association* 55 (5): 658–68. https://doi.org/10.1080/10473289.2005.10464654.

Thoning, Kirk, Ed Dlugokencky, Xin Lan, and NOAA Global Monitoring Laboratory. 2022. *Trends in Globally-Averaged CH4, N2O, and SF6*. NOAA GML. https://doi.org/10.15138/P8XG-AA10.

Tibrewal, Kushal, Philippe Ciais, Marielle Saunois, et al. 2024. "Assessment of Methane Emissions from Oil, Gas and Coal Sectors Across Inventories and Atmospheric Inversions." *Communications Earth & Environment* 5 (1): 26. https://doi.org/10.1038/s43247-023-01190-w.

Vaughn, Timothy L., Clay S. Bell, Cody K. Pickering, et al. 2018. "Temporal Variability Largely Explains Top-down/Bottom-up Difference in Methane Emission Estimates from a Natural Gas Production Region." *Proceedings of the National Academy of Sciences* 115 (46): 11712–17. https://doi.org/10.1073/pnas.1805687115.

Venkatram, Akula, and Ranga Rajan Thiruvenkatachari. 2023. "Accounting for Area Sources in Air Pollution Models." *International Journal of Environmental Research and Public Health* 20 (12): 6110. https://doi.org/10.3390/ijerph20126110.

Vesala, T., N. Kljun, Ü. Rannik, et al. 2008. "Flux and Concentration Footprint Modelling: State of the Art." *Environmental Pollution* 152 (3): 653–66. https://doi.org/10.1016/j.envpol.2007.06.070.

Wackernagel, Hans. 2003. *Multivariate Geostatistics*. Springer Berlin Heidelberg. https://doi.org/10.1007/978-3-662-05294-5.

Waxman, Eleanor M., Kevin C. Cossel, Gar-Wing Truong, et al. 2017. "Intercomparison of Open-Path Trace Gas Measurements with Two Dual-Frequency-Comb Spectrometers." *Atmospheric Measurement Techniques* 10 (9): 3295–311. https://doi.org/10.5194/amt-10-3295-2017.

Yee, Eugene, and Thomas K. Flesch. 2010. "Inference of Emission Rates from Multiple Sources Using Bayesian Probability Theory." *J. Environ. Monit.* 12 (3): 622–34. https://doi.org/10.1039/B916954G.

You, Yuan, Ralf M. Staebler, Samar G. Moussa, James Beck, and Richard L. Mittermeier. 2021. "Methane Emissions from an Oil Sands Tailings Pond: A Quantitative Comparison of Fluxes Derived by Different Methods." *Atmospheric Measurement Techniques* 14 (3): 1879–92. https://doi.org/10.5194/amt-14-1879-2021.

Zavala-Araiza, Daniel, David R. Lyon, Ramón A. Alvarez, et al. 2015. "Reconciling Divergent Estimates of Oil and Gas Methane Emissions." *Proceedings of the National Academy of Sciences* 112 (51): 15597–602. https://doi.org/10.1073/pnas.1522126112.